Healthcare Analytics 8 (2025) 100418

Contents lists available at ScienceDirect

Healthcare Analytics

journal homepage: www.elsevier.com/locate/health

A deep learning framework for 3D brain tumor segmentation and survival prediction

Ashfak Yeafi, Monira Islam *, Md. Salah Uddin Yusuf

Department of Electrical and Electronic Engineering, Khulna University of Engineering and Technology, Electrical and Electronic Engineering, Fulbarigate, Khulna, 9203, Bangladesh

ARTICLE INFO

Keywords:
Dynamic convolutional neural networks
Adversarial learning
Glioma segmentation
Radiographic data analytics
Brain tumor segmentation
Predictive analytics

ABSTRACT

Accurate and efficient segmentation of brain tumors is crucial for early diagnosis, personalized treatment planning, and improved survival rates. Brain tumors exhibit complex spatial and morphological variations, making automated segmentation a challenging task. This study introduces a dynamic segmentation network (DSNet), a novel 3D brain tumor segmentation framework that integrates adversarial learning, dynamic convolutional neural network (DCNN), and attention mechanisms to enhance precision and robustness. DSNet processes 3D magnetic resonance imaging (MRI) volumes, including T1-weighted (T1), T1-weighted with contrast enhancement (T1ce), T2-weighted (T2), and fluid-attenuated inversion recovery (FLAIR) modalities, capturing rich spatial and contextual features. Leveraging adversarial training, DSNet refines boundary definitions, while dynamic filters adapt to tumor-specific heterogeneities, ensuring accurate segmentation across diverse cases. The attention mechanism further emphasizes tumor-relevant regions, enhancing feature extraction and boundary delineation. The model was trained and validated on the BraTS 2020 dataset, achieving dice similarity coefficients of 0.959, 0.975, and 0.947 for whole tumors (WT), tumor cores (TC), and enhancing tumor (ET) regions, respectively. Its generalizability was further confirmed through evaluations on the BraTS 2019 and BraTS 2018 datasets. Additionally, volumetric features derived from segmented images were used to predict patients' overall survival rates via a Random Forest (RF) classifier. To enhance accessibility, we integrated the segmentation and prediction processes into a user-friendly web application. DSNet outperforms state-of-the-art methods, providing a robust and accurate solution for 3D brain tumor segmentation with strong clinical potential.

1. Introduction

The detection of brain tumors plays a critical role in improving patient prognosis and reducing mortality rates. Early diagnosis allows for timely intervention, which is essential for increasing survival chances and minimizing the risk of neurological damage. Brain tumors are classified into two main types: primary and secondary. The majority of primary brain tumors are gliomas, which account for more than half of all tumors internal to the cranium. The outlook for people diagnosed with brain tumors varies widely depending on their age. Those under 15 years have a 5-year survival rate of 75%, whereas individuals aged between 15 and 39 years have a 5-year survival rate of 72%, and for adults (>40 years), the rate is 72.5% [1,2]. According to the World Health Organization (WHO), gliomas are further categorized as low-grade gliomas (LGG) or high-grade gliomas (HGG), with the latter exhibiting rapid progression, greater malignancy, and increased diagnostic difficulty [3].

Medical imaging plays a central role in the detection and evaluation of brain tumors. Magnetic resonance imaging (MRI), computed tomography (CT), and ultrasound are crucial techniques for screening and diagnosing brain tumors [4]. MRI is especially beneficial among these options since it has a higher capacity to distinguish between distinct soft tissues without the need for ionizing radiation. MRI can generate high-contrast pictures in many orientations, which is extremely important for evaluating brain tumors. MRI produces four primary categories of images: Fluid-Attenuated Inversion Recovery (FLAIR), T1-weighted (T1), T1-weighted with contrast enhancement (T1ce), and T2-weighted (T2). Each category fulfills a distinct diagnostic function: T1 images are commonly employed for the identification of normal tissues, whereas T2 images are specifically designed to emphasize tumor regions. T1ce images are utilized to emphasize the borders of tumors, while FLAIR images aid in distinguishing between edema and cerebrospinal fluid (CSF) [5]. MRI's extensive imaging capabilities greatly assist physicians in diagnosing brain malignancies.

* Corresponding author.
E-mail addresses: yeafiashfak@gmail.com (A. Yeafi), monira@eee.kuet.ac.bd (M. Islam), suyusuf@eee.kuet.ac.bd (M.S.U. Yusuf).

https://doi.org/10.1016/j.health.2025.100418
Received 21 June 2025; Received in revised form 31 August 2025; Accepted 6 September 2025
Available online 17 September 2025

Accurate identification and precise quantification of tumors are crucial for improving survival rates and designing effective treatment strategies. Medical image segmentation, in particular, provides a detailed characterization of tumor morphology and spatial distribution, enabling personalized therapy and better patient outcomes [6]. Beyond segmentation, automatic detection ensures that small or heterogeneous tumors are not overlooked during diagnosis, while survival prediction delivers prognostic information that supports treatment planning, radiotherapy dose adjustment, and long-term management. Thus, detection, segmentation, and survival prediction represent interconnected clinical needs that should be addressed within a cohesive framework.

The manual process of identifying and separating brain tumors is time-consuming because it requires careful analysis of detailed medical images, such as MRI or CT scans, which contain intricate and often subtle variations in tissue structure. The complex and varied characteristics of brain tumors, including differences in size, shape, location, and texture, make it difficult for radiologists to distinguish tumors from healthy tissue accurately. Also, manual segmentation needs professional neuroradiologists [7,8]. As a result, there is growing interest in developing reliable automatic tumor detection systems.

Automatic segmentation improves the quality of the segmentation task, leading to better accuracy and reliability compared to manual methods, which are time-consuming due to the intricate details involved in identifying different tissue types. Moreover, automated systems provide a consistent and scalable solution that assists medical professionals in analyzing images more quickly and accurately [9]. In recent years, the field of medical image segmentation has seen widespread adoption of deep learning techniques. Convolutional neural networks (CNNs) are fully utilized for image segmentation have proven to be highly successful [10]. U-Net-based models have shown success in achieving proper segmentation due to integrating encoding and decoding paths into a fully convolutional framework. The U-Net architecture has emerged as a fundamental framework for creating automated systems that improve the precision and effectiveness of brain tumor segmentation due to its ability to capture both local and contextual information [11]. Despite this progress, conventional CNNs still face limitations in capturing fine-grained boundaries and the complex spatial characteristics of tumors.

For enhanced segmentation precision, volumetric segmentation models offer a compelling solution by capturing spatial continuity across MRI slices, which is especially crucial for 3D medical imaging tasks [12]. These models mitigate the class imbalance that frequently arises from the small tumor regions compared to the larger brain volume, ensuring a more balanced representation of tumor and non-tumor areas. However, the static nature of traditional CNN filters can hinder their ability to adapt to the complex, heterogeneous structure of brain tumors [13]. Dynamic convolution is employed to overcome these limitations, as it allows for adaptive filtering that more effectively captures tumor-specific features across diverse images, thereby enhancing segmentation accuracy [14].

In recent years, adversarial learning has also shown potential in refining segmentation outcomes by enhancing boundary sharpness and realism [15]. In adversarial frameworks, a generator network (such as a segmentation model) and a discriminator network engage in a competitive process, whereby the generator aims to produce realistic segmentations while the discriminator works to identify inconsistencies [16]. This adversarial process helps sharpen segmentation boundaries and better distinguish tumor regions from surrounding tissues. Previous work, such as U-Net Generative Adversarial Network (U-Net-GAN) [17], has shown that integrating adversarial learning with segmentation models can improve segmentation outcomes by enhancing detail and boundary accuracy.

Based on these insights, we propose a dynamic segmentation network (DSNet), a novel deep learning framework for 3D brain tumor analysis. DSNet integrates dynamic convolution and adversarial learning to improve segmentation precision and robustness, while also incorporating tumor detection and survival prediction into a unified system. Specifically, DSNet addresses the three clinical gaps: (i) tumor detection ensures that small and heterogeneous tumors are identified early, reducing the likelihood of missed diagnoses; (ii) fine-grained segmentation provides accurate delineation of tumor boundaries; and (iii) survival prediction using volumetric features, ensuring both diagnostic accuracy and prognostic utility for clinical practice. Unlike prior works that focus solely on segmentation, DSNet bridges diagnostic and prognostic needs, thereby offering a clinically meaningful solution. The framework is trained on the BraTS 2020 dataset and validated on the BraTS 2019 and 2018 datasets, demonstrating robust generalizability and accuracy across different tumor subtypes. The overall contribution of our work is stated below:

- Present a 3D segmentation model that improves tumor detection in multimodal medical imaging.
- Leverage deep learning and attention mechanisms to increase accuracy in brain tumor segmentation.
- Validate model effectiveness using benchmark medical datasets for real-world relevance.
- Integrate a survival prediction tool combining imaging and clinical data for prognosis support.
- Deliver a user-friendly interface to support clinicians in diagnostic and treatment planning workflows.

The following sections are presented as follows:

Section 2 provides a comprehensive review of prior research on brain tumor segmentation and survival prediction, highlighting key advancements and gaps in the field. Section 3 outlines the datasets and methodologies employed in this study, detailing the experimental setup and design. The results of the simulations are presented in Section 4, with a thorough analysis divided into multiple subsections that address each dataset individually and include a comparative evaluation against established state-of-the-art methods using the primary dataset. Section 5 presents an in-depth discussion of the findings, contextualizing their implications within the broader research domain. Finally, Section 6 concludes the article by summarizing the contributions and significance of the study. The comprehensive methodology of our study is shown in Fig. 1.

2. Literature review

Brain tumor segmentation is a vital step in the clinical pipeline for accurate diagnosis, prognosis, and treatment planning [18]. Traditional methods, such as threshold-based and region-based approaches, primarily rely on handcrafted features and pixel intensity levels to identify tumors. While these methods have shown some success in simpler cases, they struggle to handle the inherent complexity, heterogeneity, and noise in MRI data, often resulting in suboptimal performance [19]. In recent years, neural networks have emerged as a transformative technology for medical image segmentation, providing a significant leap forward in precision and scalability. Encoder–decoder architectures, such as the U-Net model, have become the cornerstone of medical image segmentation due to their ability to learn both global and local features effectively [11,20]. The U-Net architecture combines a contracting path for feature extraction and an expansive path for feature reconstruction, enabling it to capture multi-scale information. Its success has inspired numerous variants tailored to address specific challenges in medical imaging. For instance, U-Net++ introduces nested skip pathways to improve feature refinement [21], while Attention U-Net incorporates attention mechanisms to focus on critical regions of interest, such as tumor boundaries [22]. Other notable variants include Residual U-Net (Res-U-Net), which integrates residual connections for improved gradient flow [23], and lightweight U-Nets, which reduce computational costs without significantly compromising segmentation accuracy [24]. Walsh et al. [24] introduced a lightweight

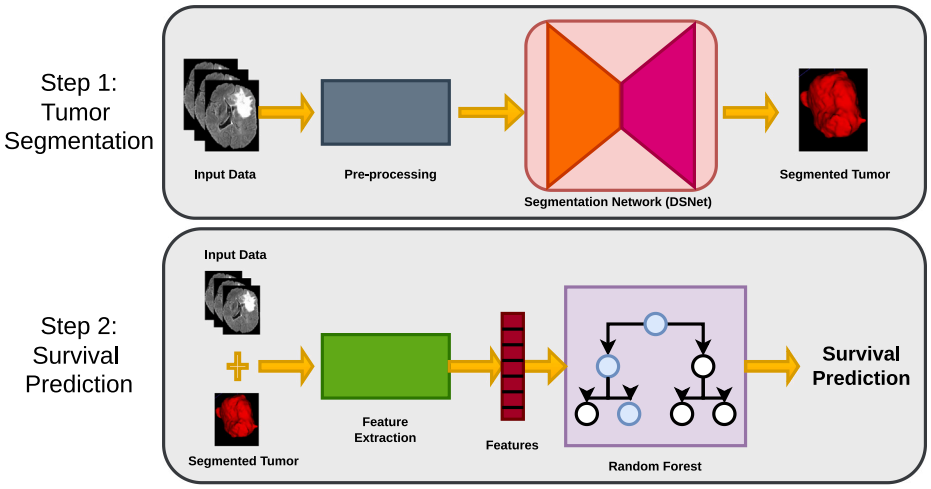

Fig. 1. Block diagram of the proposed DSNet-based framework, comprising two main stages: (a) brain tumor segmentation using a deep learning model, and (b) patient survival prediction based on extracted imaging and clinical features.

U-Net architecture that segments brain tumors using 2D MRI slices from three orthogonal planes, eliminating the need for large datasets and data augmentation while maintaining strong performance for real-time applications. Tseng et al. [25] developed an automated detection method based on an optimized eXtreme Gradient Boosting (XGBoost) model, incorporating Contrast Limited Adaptive Histogram Equalization (CLAHE) for image enhancement, K-Means for segmentation, and Particle Swarm Optimization (PSO) for feature selection, with classification performed using XGBoost, Naive Bayes, and Iterative Dichotomiser 3 (ID3). Lamba et al. [26] proposed an integrated approach combining deep learning and supervised learning, utilizing data augmentation, a Visual Geometry Group 16-layer network (VGG16) with transfer learning for feature extraction, and a linear Support Vector Machine (SVM) for accurate classification, showing strong diagnostic capability on public MRI datasets. Despite the success of 2D CNNs, they are inherently limited in capturing the three-dimensional spatial context of MRI data. To address this, 3D CNN architectures, such as 3D U-Net [27], have been proposed. These models replace 2D convolutions with 3D convolutions, enabling the direct extraction of volumetric features from MRI scans. Another promising line of research involves generative adversarial networks (GANs), which have demonstrated substantial potential in generating high-quality segmentation masks [28]. GANs employ a generator and a discriminator in an adversarial setup, where the generator learns to produce realistic segmentation outputs, and the discriminator evaluates their authenticity. A 3D GAN model named Voxel-to-Voxel GAN (Vox2Vox), which combines a U-Net-based generator with a CNN-based discriminator, has achieved competitive results in brain tumor segmentation tasks [29]. Peiris et al. proposed a reciprocal GAN framework with virtual adversarial training and critic modules to enhance robustness and reduce prediction errors [30]. While CNNs and GANs dominate the field, attention mechanisms and transformer-based models are emerging as powerful alternatives due to their ability to capture long-range dependencies. Recent studies have explored hybrid architectures combining CNNs with transformers to improve the segmentation of complex and heterogeneous tumor regions [31]. These methods demonstrate improved performance, particularly in handling large variations in tumor size and morphology. Despite these advancements, several challenges persist. Existing methods often struggle with class imbalance, where underrepresented tumor subtypes such as glioblastoma receive less accurate segmentation [32]. Furthermore, high dependency on large annotated datasets limits their scalability, especially in low-resource settings. In this study, we build upon these advancements by introducing a novel approach that integrates dynamic convolutional neural networks, attention mechanisms, and adversarial learning into a unified framework.

3. Materials and methods

3.1. Datasets

Our study leveraged the Multimodal Brain Tumor Image Segmentation Benchmark (BraTS) datasets from 2018, 2019, and 2020 [33–35]. The BraTS 2020 dataset primarily served as the training foundation for our model, while the BraTS 2019 and BraTS 2018 datasets were incorporated to assess model generalizability. Each of these datasets comprises MRI scans depicting glioma-affected brain areas, with a voxel resolution of $1 \times 1 \times 1$ mm^3 and initial volume dimensions of $240 \times 240 \times 155$. The scans include four MRI modalities: T1, T1ce, T2, and FLAIR. Ground truth annotations are assigned values of 0, 1, 2, and 4, where 0 represents non-tumor regions, and 1, 2, and 4 signify distinct tumor regions, specifically categorized for segmentation tasks as the tumor core (TC), whole tumor (WT), and enhancing tumor (ET).

For model training, we selected 176 samples from the 'BraTS2020 TrainingData' folder, which comprises 369 samples in total. These samples were chosen using a 5-fold stratified k-fold method to ensure balanced representation. Stratified k-fold cross-validation was selected to maintain a proportional representation of class distributions within each subset, mitigating potential biases and improving the reliability of our results [36]. One fold, containing 44 samples, was reserved as a validation set to maintain consistent evaluation metrics across experiments. Among the 369 cases, 118 included additional details such as age, resection status (Gross Total Resection (GTR)), and survival duration. A survival estimation model was built using this subset. The validation dataset for survival analysis was a subset of the segmentation validation set, comprising images from 29 patients with GTR status and age information, while the test dataset included 107 cases. Furthermore, we employed the BraTS 2019 and BraTS 2018 datasets to evaluate our model's cross-dataset performance. BraTS 2019 includes MRI scans from 259 HGG patients and 76 LGG patients, while BraTS 2018 contains scans from 210 HGG and 75 LGG cases. For our specific segmentation objectives, only HGG samples from the 2019 and 2018 datasets were used, allowing for a focused analysis on high-grade tumor detection. The inclusion of these additional datasets enabled a comprehensive evaluation of the model's performance across diverse glioma cases, thereby ensuring its reliability and generalizability across various datasets.

3.2. Data pre-processing

We have applied center cropping to every image to increase the learning efficacy of our network and reduce computational requirements. Fig. 2 depicts the center cropping method, in which the training

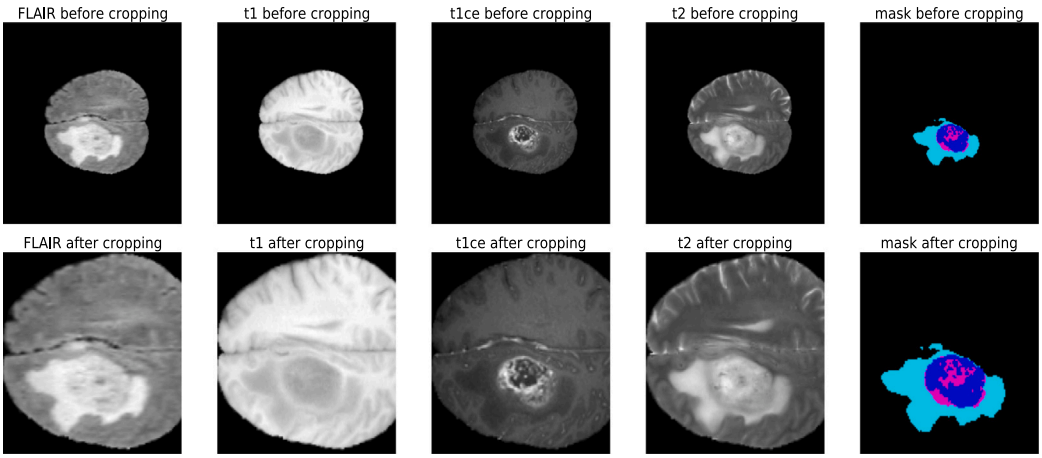

Fig. 2. The 100th slice of ID 'BraTS20_Training_140'. The first row displays the unprocessed image, while the second row exhibits the image after undergoing processing.

only focuses on the core region of each image while excluding the outlying sections. This method focuses on the specific areas of interest (ROIs) in the image, as the outer areas typically include unimportant information that could negatively impact the performance of the network. Our dataset consists of centrally positioned MRI scans, which include tumors and their corresponding regions. As a result, this cropping method allows the network to concentrate on important characteristics, hence improving the accuracy of segmentation [37].

The scans were reshaped from their original dimensions to a resolution of 128 × 128 × 128, resulting in a total of 2,097,152 pixels per voxel image. In addition, this scaling allowed us to train our network efficiently despite the limitations of our GPU resources. In Fig. 2, the column on the right displays the accurate representation of the three classes (WT: cyan, TC: navy blue, ET: magenta). Both masks and images are cropped in the same way. In this study, no additional data augmentation techniques were employed beyond center cropping. This decision is supported by prior evidence indicating that, for medical imaging tasks involving brain tumors, deep learning models often achieve higher reliability and diagnostic accuracy when trained on minimally processed or raw MRI scans, as opposed to heavily augmented datasets [38–40].

3.3. Segmentation

3.3.1. Network fundamentals

Our proposed segmentation network (DSNet) is constructed with a dynamic convolutional neural network (DCNN) layer, as proposed in [14]. The structure of DCNN is shown in Fig. 3. At first, the 3D adaptive average pooling layer compresses the spatial information [41]. Two 3D convolution layers (Conv3D) process the input. The first Conv3D layer is followed by a Rectified Linear Unit (ReLU) activation, while the second Conv3D layer is followed by a softmax activation. This produces normalized attention weights for the convolution kernels. Once we finish the aggregated convolution and calculate the attention, we pass the output through a Conv3D layer. Features generated by 3D convolution contain a greater amount of spectral information due to the additional dimension of the 3D convolution layer. 3D convolution can be formalized by the Eq. (1). It gives the value at the point (x, y, z) of the j^th feature map in the i^th convolution layer [42].

$$P_{i,j}^{x,y,z} = f\left(\sum_{m}\sum_{h=0}^{H_i-1}\sum_{w=0}^{W_i-1}\sum_{d=0}^{D_i-1} k_{i,j,m}^{h,w,d} P_{(i-1),m}^{(x+h),(y+w),(z+d)} + v_{i,j}\right) \tag{1}$$

The value of $k_{i,j,m}^{h,w,d}$ represents the element at position (h, w, d) in the kernel associated with the mth feature map in the previous layer. D_i represents length of the 3D kernel in the temporal dimension.

We used the 3D max pooling technique (MaxPool3D) [43] to perform the pooling operations. The operation of MaxPool3D can be expressed with Eq. (2).

$$\text{out}\left(H_{in}, W_{in}, D_{in}\right) = \max_{p=0,\ldots,\rho H-1}\ \max_{m=0,\ldots,\rho W-1}\ \max_{n=0,\ldots,\rho D-1} \tag{2}$$

where H_{in}, W_{in}, D_{in} are input height, width and depth respectively, and $(\rho H, \rho W, \rho D)$ is the kernel size. This layer not only decreases the spatial dimensions of the feature maps but also decreases the number of parameters and computational expenses.

In addition, we employed the approach of 3D batch normalization (BatchNorm3D) [44] for the purpose of regularization. Batch normalization is computed using Eq. (3).

$$y = \gamma * \frac{x_i - \mu_b}{\sqrt{\sigma_b^2 + \epsilon}} + \beta \tag{3}$$

In this case, x_i represents the input received from the ith batch, while y represents the result after the normalization process. The symbol μ_b denotes the average value of a batch, and σ_b^2 reflects the measure of dispersion within a batch. The symbols γ and β are parameters that can be adjusted, whereas ϵ is a small constant that is included to avoid division by zero.

Skip connections are a way to design deep neural networks that allow for the bypassing of certain layers. This solves the vanishing gradient problem by enabling direct access to previous features and facilitating the flow of gradients back through the input during backpropagation. [45]. In our DSNet structure, we have implemented an attention-based skip connection. We changed the attention mechanism suggested in [46] and swapped out the standard convolutional layer for a DCNN. Now, our process takes a query and a set of key–value pairs and turns them into an output, which is a weighted sum of values. The attention mechanism determines the weighting factors by assessing the compatibility between the query and its corresponding key. Fig. 4 shows how we implemented the attention-based skip connection. The attention technique lets the decoder network get important data from the encoder network. This is important for making the segmentation mask of the upsampled features better and more accurate.

In constructing our segmentation model, we employed three distinct activation functions: ReLU, leaky rectified linear unit (Leaky ReLU), and Softmax. The ReLU feature enhances training speed by allowing positive values to pass, enhancing non-linearity without increasing computation difficulty, as defined in Eq. (4) [47].

$$f(p) = max(0, p) \tag{4}$$

Here p is the input value.

We incorporate Leaky ReLU [48], a second activation function, to address potential issues with traditional ReLU, such as dying neurons,

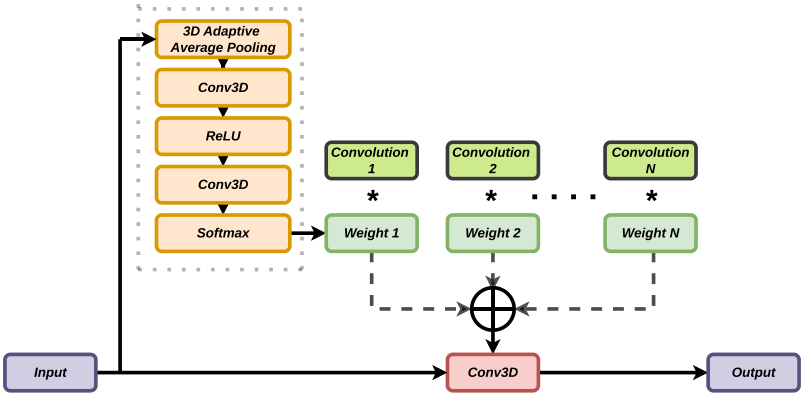

Fig. 3. Dynamic convolution neural network (DCNN) structure.

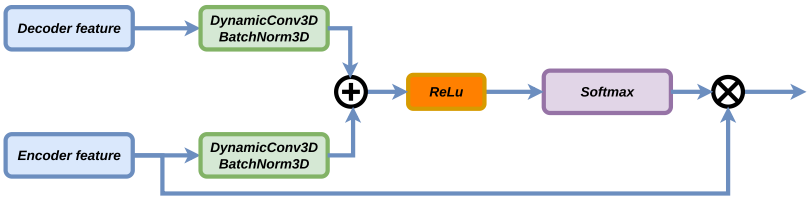

Fig. 4. Illustration of the attention mechanism structure implemented in DSNet's skip Connections.

by allowing a small, non-zero gradient. For a given input p, Leaky ReLu is mathematically expressed by Eq. (5).

$$f(p) = max(0.01 \times p, p) \tag{5}$$

In order to handle multi-class classification tasks, we added the Softmax [49] activation function to the output layer. This function changes output logits into probability distributions over multiple classes. Eq. (6) mathematically explains the softmax activation function.

$$y_i = \frac{\sigma^{(p_i)}}{\sum_{j=1}^{N} \sigma^{(p_j)}} \tag{6}$$

where N indicates the total number of classes, p_i represents the ith member of the input vector p, σ denotes the base of the natural logarithm, and the denominator ensures that the total probabilities sum up to 1.

3.3.2. Proposed model

Our proposed network design comprises two modules: a segmentation network named DSNet and a critic network. The collaboration of these components results in the accurate segmentation of medical imaging data. Our proposed workflow for the segmentation task is shown in Fig. 5.

The architecture of DSNet consists of a 3D U-Net structure, which includes a 5-level encoder and a corresponding 5-level decoder. The DSNet architecture relies heavily on the implementation of a DCNN. Our proposed encoder consists of repeating Residual Double Convolution (ResDoubleConv) blocks. Each block consists of 3D DCNN layers, 3D batch normalization layers, and Leaky ReLU activation layers. Fig. 6 illustrates the structure of the ResDoubleConv block. ResDoubleConv blocks integrate residual connections to improve the network's information flow and address issues such as the vanishing gradient problem [45]. As a result, training becomes more effective, leading to improved convergence and performance. The encoder is made of multiple ResDoubleConv blocks, each of which is isolated using a MaxPool3D layer with a kernel size of $2 \times 2 \times 2$ and a stride of $2 \times 2 \times 2$. This layer performs batch downsampling with a reduction factor of 2. We specifically designed the block layout to aid in the extraction of higher-level features, thereby enhancing the network's overall accuracy.

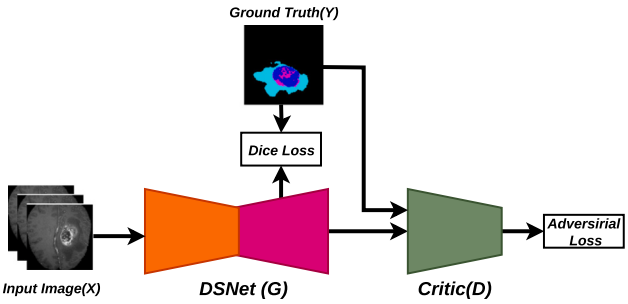

Fig. 5. Proposed overall network architecture for segmentation: The diagram illustrates the segmentation network (DSNet) and the critic network, denoted by G and D, respectively. Input data (X) and ground truth segmentation masks (Y) are also depicted.

In the DSNet decoder unit, an upsampling layer follows the ResDoubleConv block. We arrange the blocks sequentially, and the upsampling layer uses the 'Nearest Neighbor' [50] method to increase the data size by a factor of 2. We couple the encoder and decoder in series, using attention-based skip connections to link the levels together. The mechanism of our attention-based skip connection is described in Section 3.3.1. The final configuration of DSNet is seen in Fig. 7.

We designed the critic network as a fully convolutional adversarial network specifically to improve the segmentation network's performance. The critic network employs 3D convolutions, which are essential for handling volumetric input and capturing spatial relationships in three dimensions. We use the critic architecture, which is based on the Markovian PatchGAN [51,52] architecture. The Markovian PatchGAN architecture is well-known for its ability to provide confidence ratings for prediction masks based on the assessment of local patches of the input rather than the complete image. This patch-based technique allows the network to concentrate on fine details and local coherence, which is advantageous for tasks that require accurate segmentation at high resolution. The structure of our critic network is depicted in

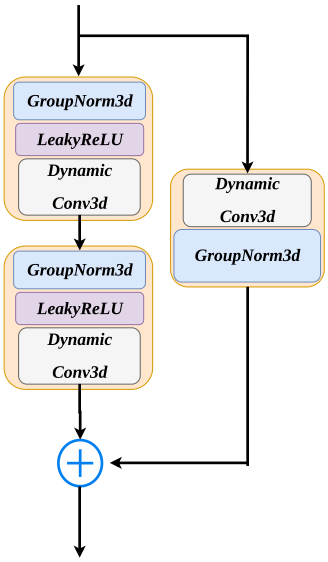

Fig. 6. Illustration of the ResDoubleConv block implemented in DSNet's encoder–decoder architecture. This block combines residual connections with dynamic convolutional layers to enhance feature extraction and network performance.

Fig. 8. The construction consists of four conjugative, completely three-dimensional convolutional layers. The critic's main role is to guide the DSNet network into producing accurate segmentation masks.

3.3.3. Loss function

Our segmentation network learns through an adversarial learning process. The optimization of our network can be formalized through a min–max problem

$$\min_{G} \max_{D} L(G; X) \tag{7}$$

where G is the DSNet model parameter and D is the critic model parameter. The overall loss of our proposed model consists of two terms,

$$L(Y; X) = \alpha L_{Dice}(G; X) + \beta L_{Adv}(G; D; X) \tag{8}$$

where L_{Dice} and L_{Adv} represent dice loss and adversarial loss. α, β are weights assigned to them. Dice loss depends on the segmentation network, and adversarial loss is defined based on the parameter of the entire model. If we choose these parameters appropriately within a tolerable range, the segmentation network demonstrates strong functionality and exhibits generalization capabilities. In our experiments, we set the values of α and β to 0.5 each.

We use dice loss for the segmentation network, represented by Eq. (9).

$$L_{Dice}(G; X) = 1 - \frac{2\hat{Y} + 1}{Y + \hat{Y} + 1} \tag{9}$$

where Y represents the true segmentation and $\hat{Y}$ represents the predicted segmentation. We add 1 as a smoothing value in the numerator and the denominator to prevent the formula from becoming undefined in edge-case scenarios. The adversarial loss refers to the measurement of the discrepancy between the predicted distribution and the actual distribution. It is defined in Eq. (10).

$$L_{\text{Adv}}(G; D; X) = \mathbb{E}_{(X,Y)\sim p_{\text{data}}} \left[-\sum_{a\in H} \sum_{b\in W} \Big((1-\eta) \log\big(D(X)\big) + \eta \log\big(1 - D(G(X))\big) \Big) \right] \tag{10}$$

Algorithm 1 DSNet: Training and Inference

Require: MRI dataset $\{(X, Y, T, E)\}$; Generator G (Conv3D + Attention + DCNN); Discriminator D; loss $\mathcal{L}_{Dice}$; weight λ
Ensure: Trained G, D, survival model S
Training:
for each batch (X, Y, T, E) **do**
  Preprocess MRI, extract ROI via coarse detection
  Predict mask $\hat{Y}_{roi} \leftarrow G(X_{roi})$
  Compute segmentation loss $\mathcal{L}_{Dice}(\hat{Y}, Y)$
  Compute adversarial loss with D
  Update D then update G with $\mathcal{L}_{Dice} + \lambda \mathcal{L}_{Adv}$
  Extract features from $\hat{Y}$ for survival set $\mathcal{F}$
end for
Train survival model S on $\mathcal{F}$ (e.g., Cox/RSF)
Inference:
Preprocess test X, detect ROI, predict $\hat{Y} = G(X_{roi})$
Post-process segmentation; if S exists, compute risk $\hat{r} = S$(features)
return $\hat{Y}, \hat{r}$

where the indices H and W correspond to the height and width dimensions of the image. $\mathbb{E}_{(X,Y)\sim p_{\text{data}}}$ denotes the expectation taken over the data distribution p_{data}, with X representing the input images and Y representing the corresponding ground-truth labels. The parameter η balances the contribution of real and generated images in the adversarial loss. When $\eta = 0$, the segmentation model generates the sample. In contrast, when $\eta = 1$, the sample is derived directly from the true underlying data. The segmentation network employs adversarial loss to generate predictions that closely resemble the actual masks, intending to deceive the critic.

3.4. Survival prediction

In this study, survival prediction is approached as a classification task based on manually defined survival categories, designed to reflect varying levels of severity. The dataset is stratified into three discrete classes: short-term survival (0–300 days), mid-term survival (301–450 days), and long-term survival (> 450 days). These thresholds are not derived from clinical standards or WHO guidelines, as no standardized day-based survival benchmarks exist. Instead, this categorization is introduced to enable a structured and interpretable analysis of survival outcomes.

For feature extraction, we leverage the output from the segmentation model to compute volumetric features corresponding to different tumor subregions (e.g., enhancing tumor, tumor core, whole tumor). These volume-based metrics capture critical spatial characteristics of the tumors. Additionally, patient age is incorporated as a clinical feature known to influence survival. The combined feature set — comprising both volumetric and demographic data — is used to train and evaluate various machine learning classifiers, aiming to identify the most effective model for predicting survival categories. In addition to these classification-based approaches, we also incorporated a time-to-event modeling framework using DeepSurv [53], a neural-network-based extension of the Cox proportional hazards model. This approach models the hazard function directly, accounts for censored data, and enables estimation of hazard ratios and survival curves, providing complementary prognostic insight beyond discrete classification. The schematic diagram illustrating the proposed approach for survival prediction can be found in Fig. 1 (Step:2).

The overall DSNet workflow, including training and inference, is summarized in Algorithm 1.

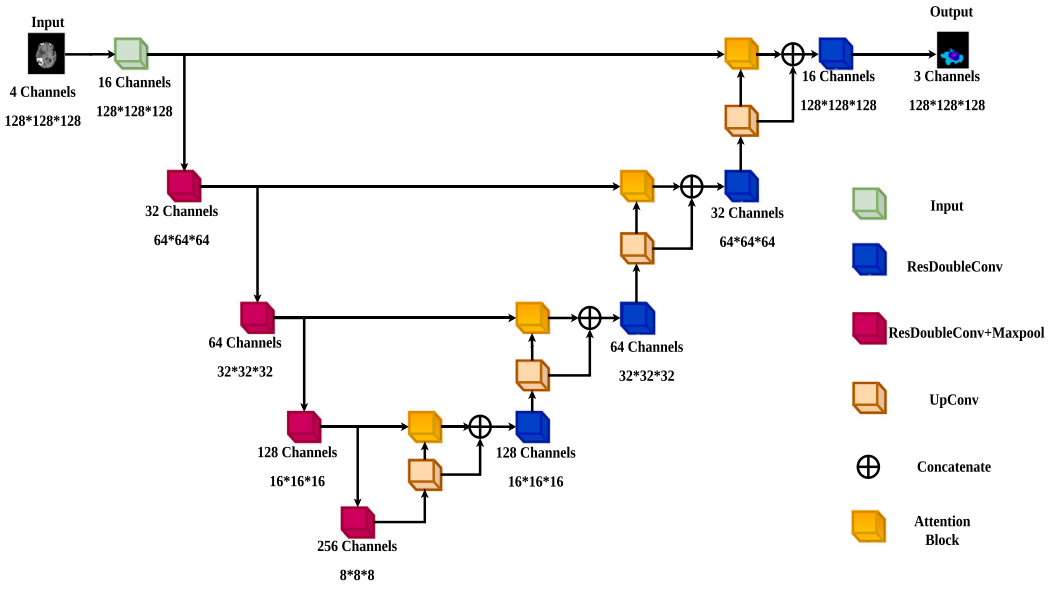

Fig. 7. Our proposed DSNet segmentation model architecture.

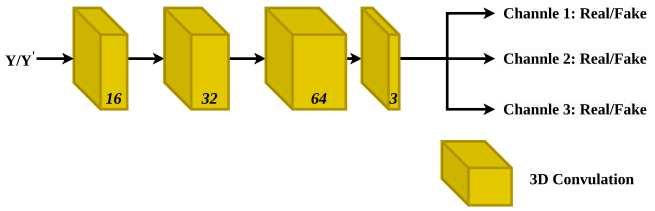

Fig. 8. Critic model architecture.

4. Results analysis

4.1. Hardware and training protocol

We established our training environment by utilizing Python (version 3.9.19) and the PyTorch framework (version 1.6.0). We conducted the experiments on a Windows 10 system with 64 GB of RAM, utilizing the 'torch' module. We trained the segmentation network for 250 epochs using a batch size of 2. In DSNet, we employed the Adaptive Moment Estimation with Weight Decay (AdamW) optimizer [54] with a learning rate of 0.0002. The critic network was trained using the Root Mean Square Propagation (RMSprop) optimizer [55], with a learning rate of 0.00005. We determined these hyperparameters through experimentation and the selection of values that produced optimal results. We maintained all other optimizer settings at their default values without making any additional adjustments. We chose these modest learning rates to prevent problems with local minima, hence ensuring more steady convergence during the training process [56]. This methodology resulted in outcomes that were more dependable and precise.

4.2. Evaluation metrics

The Dice Similarity Coefficient (DSC) is a similarity metric commonly employed to assess the effectiveness of image segmentation algorithms. DSC is calculated by multiplying the intersection of the ground truth data and the segmented image by 2 and then dividing the result by the sum of their sizes [57]. This is expressed mathematically in Eq. (11).

$$DSC(k,\hat{k}) = \frac{2|k \cap \hat{k}|}{|k| + |\hat{k}|} \tag{11}$$

The Jaccard Index, or Intersection over Union (IoU) score, is also a similarity metric used to compare the diversity of sample sets. Like DSC, the intersection of the aforementioned sets is used, but in this case, it is divided directly by their union as shown in Eq. (12) [57].

$$IoU(k,\hat{k}) = \frac{|k \cap \hat{k}|}{|k \cup \hat{k}|} \tag{12}$$

Eqs. (11) and (12) both include a ground truth segmentation denoted as k, and a predicted segmentation denoted as $\hat{k}$. Both DSC and IoU scores range from 0 (complete mismatch) to 1 (perfect match).

The sensitivity (Sen), represented by Eq. (13), is a widely used metric for assessing the effectiveness of image segmentation algorithms [58]. It quantifies the accuracy of identifying genuine positive pixels.

$$Sen = \frac{True\ positives}{True\ positives + False\ negatives} \tag{13}$$

A high Sen score indicates that the algorithm is good at detecting objects in the image, while a low Sen score means that many object pixels were missed or incorrectly identified as background.

4.3. Segmentation results

The segmentation task was conducted using the BraTS 2020 dataset. We adopted a U-Net-type architecture with an equal number of encoder and decoder units to optimize feature extraction and reconstruction across scales. This balanced structure enhances spatial detail retention during downsampling and upsampling, which is crucial for accurate segmentation boundaries in medical imaging. Additionally, maintaining symmetry between encoder and decoder units supports stable gradient flow, improving the model's ability to capture fine details [59,60]. To identify the most effective architecture, we evaluated multiple DSNet configurations with varying depths and stages. Through comparative analysis, we selected the DSNet structure that offered the best balance between segmentation accuracy and parameter efficiency. In Table 1, we present the segmentation performance and model parameters for DSNet across different stage configurations (4, 5, and 6 stages) after training for 50 epochs. We evaluated segmentation accuracy using IoU and DSC scores for the WT: Cyan, TC: Navy Blue, ET: Magenta regions. As observed, the 5-stage DSNet configuration achieved the best balance between segmentation accuracy and model complexity, producing IoU scores of 0.837 for WT, 0.856 for TC, and

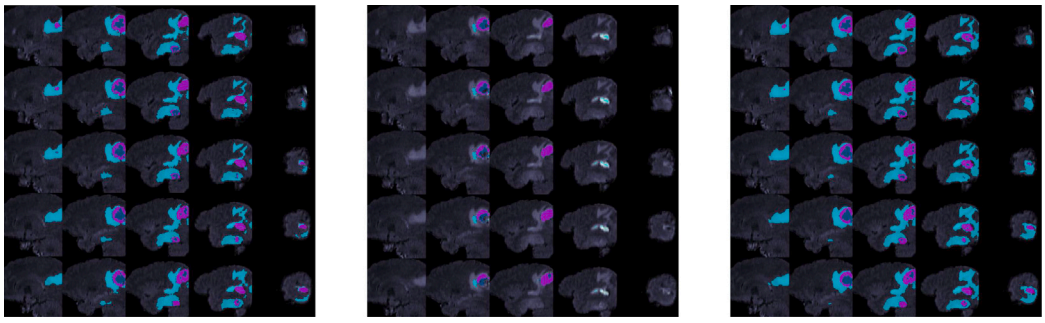

(a) Ground Truth (b) Without Skip Connection (c) With Skip Connection

Fig. 9. Segmentation results for case **BraTS20_Training_024**. (a) Ground truth segmentation mask, (b) DSNet prediction without skip connections, and (c) DSNet prediction with skip connections. Tumor subregions are color-coded as follows: WT (Cyan), TC (Navy Blue), and ET (Magenta).

Table 1
Comparison of coefficient scores (IoU and DSC) for each segmentation class (WT, TC, and ET) across different DSNet stages (4, 5, 6). The final row displays model parameter counts for each stage configuration.

		4 Stage	5 Stage	6 Stage
IoU	WT	0.782	0.837	0.834
	TC	0.803	0.856	0.863
	ET	0.692	0.742	0.753
DSC	WT	0.842	0.909	0.908
	TC	0.851	0.922	0.925
	ET	0.784	0.844	0.854
Parameters		7.97M	31.96M	128M

0.742 for ET. In terms of DSC, the 5-stage model performed similarly well, yielding values of 0.909, 0.922, and 0.844 for WT, TC, and ET, respectively. Although the 6-stage network marginally outperformed the 5-stage model in certain classes, its parameter count (128M) was substantially higher than that of the 5-stage model (31.96M). This increase in complexity and computational demand led us to select the 5-stage DSNet as the optimal architecture, as it balances high segmentation performance with manageable computational costs. The 4-stage model, while more parameter-efficient (7.97M), exhibited lower segmentation accuracy across all classes.

Furthermore, we discovered that adjusting the skip connections according to the contextual levels of the encoder-to-decoder relationship produced the most precise outcomes. More precisely, we found that a symmetrical link between the encoder and decoder, which immediately sends the outputs at each level of the encoder to an attention unit, led to improved performance. Figs. 9(a)–9(c) illustrate the segmentation outcomes of DSNet trained with and without skip connections over 50 epochs. These results clearly indicate that incorporating skip connections enhances segmentation accuracy compared with their absence.

To justify the choice of the DSNet architecture, an ablation study was performed in Table 2 comparing four configurations: (i) a baseline 3D CNN, (ii) a 3D CNN with attention skip connections, (iii) a 3D CNN with both attention skip connections and DCNN modules, and (iv) the full DSNet incorporating an integrated critic network. All models were trained for 50 epochs on the BraTS 2020 dataset. The results demonstrated progressive improvements with the addition of each component, thereby validating the effectiveness of the complete 3D DSNet framework.

Figs. 10(a) and 10(b) depict the dice and adversarial loss curves obtained by training our model using the BraTS 2020 dataset for 250 epochs. The adversarial loss and the total segmentation loss are decreasing. The coefficient scores, depicted in Figs. 11(a) and 11(b), illustrate the efficacy of our proposed approach. Using DSC, we successfully managed the difference between the foreground and background.

After 250 epochs, our proposed network achieved a DSC of roughly 0.96 and an IoU of over 0.92 on the validation set. Table 3 presents a comprehensive examination of individual performance results for each of the three classes. Although there was a possibility of class imbalance biasing the network, our model achieved excellent performance across all classes. The WT region exhibited a DSC of around 0.959, an IoU of 0.923, and a SEN score of 0.952, suggesting strong segmentation performance with minimal false negatives. In the TC and ET zones, the Sen scores exhibited a high level of performance, whereas the IoU levels were quite moderate. Nevertheless, the DSC scores remained remarkable, earning a score of 0.975 for TC segmentation and 0.947 for ET area segmentation.

The quality of the predicted masks generated by our model is illustrated in Fig. 12 for patients BraTS20_Training_001, BraTS20_Training_006, and BraTS20_Training_069 from the BraTS 2020 dataset. In the figure, there are 20 images in each batch, which are segments of a single MRI image. The figure depicts both the real segmentation masks and the predicted results derived from our model. The high degree of similarity between the predicted outcomes and the original ground truth supports the accuracy of our method. We were able to reliably identify the shapes within each category, particularly in the WT region, with minimal variations. The model's exceptional segmentation accuracy demonstrates its effectiveness.

We trained our model using the BraTS 2019 and BraTS 2018 datasets, as shown in Fig. 13 and Fig. 14, respectively. The training and validation curves depicted in these images exhibit tendencies similar to those observed with the BraTS 2020 dataset. Despite training our model primarily on the BraTS 2020 dataset, it has achieved impressive outcomes for both BraTS 2019 and BraTS 2018. Our model demonstrated exceptional performance, with DSC values nearing 0.96 for both datasets, indicating a high level of accuracy. The loss values were low, highlighting the effectiveness of the approach.

Table 3 displays the comprehensive DSC scores for each of the three classes, as well as the overall validation accuracy. We found that the DSC values for the WT, TC, and ET areas are 0.956, 0.972, and 0.93 for BraTS 2019, 0.962, 0.973, and 0.948 for BraTS 2018. According to the BraTS 2020 study's findings, the scores for ET segmentation are somewhat lower. The inherent imbalance in the dataset explains this. These results confirm that our network is skilled at training with fresh data and achieves high levels of accuracy.

To evaluate the generalization capability of DSNet, we trained the model on the BraTS 2020 dataset and validated its performance using the BraTS 2019 and BraTS 2018 datasets. Table 4 illustrates the performance metrics, including DSC, IoU, and SEN across three tumor regions: WT, TC, and ET. The results demonstrate that DSNet achieves consistent and high segmentation performance across datasets, indicating its robustness and ability to generalize to unseen data. Specifically, the model achieved DSC scores of 0.946, 0.942, and 0.919 for WT, TC,

Table 2
Ablation study results showing the impact of different components in the proposed DSNet architecture. Performance is reported using DSC, IoU, and Sen for WT, TC, and ET segmentation.

		WT	TC	ET
3D CNN	DSC	0.883	0.858	0.806
	IoU	0.796	0.794	0.690
	Sen	0.879	0.902	0.881
3D CNN + Skip Connections	DSC	0.887	0.873	0.812
	IoU	0.802	0.783	0.697
	Sen	0.908	0.888	0.878
3D CNN + Skip Connections + DCNN modules	DSC	0.896	0.917	0.843
	IoU	0.814	0.849	0.739
	Sen	0.910	0.927	0.913
DSNet (3D CNN + Skip Connections + DCNN + critic network)	DSC	0.901	0.923	0.876
	IoU	0.853	0.870	0.784
	Sen	0.927	0.931	0.922

Table 3
Coefficient scores (mean ±SD) obtained for each separate class after training with BraTS 2020, BraTS 2019, and BraTS 2018 datasets after 250 epochs. Including standard deviations improves the robustness and credibility of the reported results.

		WT	TC	ET
BraTS 2020	DSC	0.959 ± 0.012	0.975 ± 0.010	0.947 ± 0.015
	IoU	0.923 ± 0.014	0.951 ± 0.013	0.901 ± 0.018
	Sen	0.952 ± 0.011	0.977 ± 0.009	0.970 ± 0.013
BraTS 2019	DSC	0.956 ± 0.013	0.972 ± 0.012	0.930 ± 0.016
	IoU	0.916 ± 0.015	0.945 ± 0.014	0.872 ± 0.019
	Sen	0.939 ± 0.012	0.982 ± 0.008	0.984 ± 0.010
BraTS 2018	DSC	0.962 ± 0.011	0.973 ± 0.010	0.948 ± 0.014
	IoU	0.926 ± 0.013	0.949 ± 0.012	0.903 ± 0.017
	Sen	0.952 ± 0.010	0.968 ± 0.011	0.978 ± 0.012

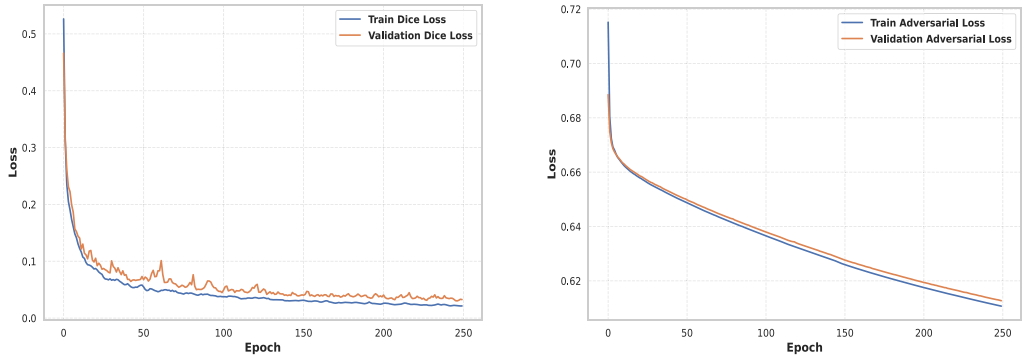

(a) (b)

Fig. 10. Loss curves obtained from training the proposed model for 250 epochs on the BraTS 2020 dataset: (a) Dice loss and (b) Adversarial loss.

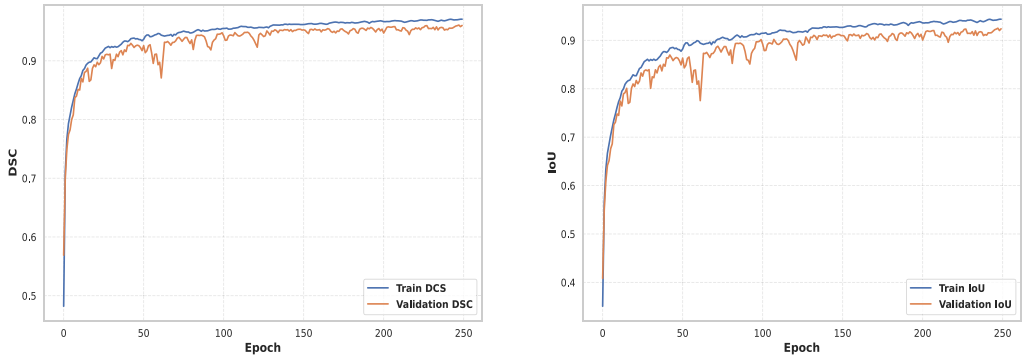

(a) (b)

Fig. 11. Evaluation metrics obtained from training the proposed model for 250 epochs on the BraTS 2020 dataset: (a) Dice Similarity Coefficient (DSC) and (b) Intersection over Union (IoU).

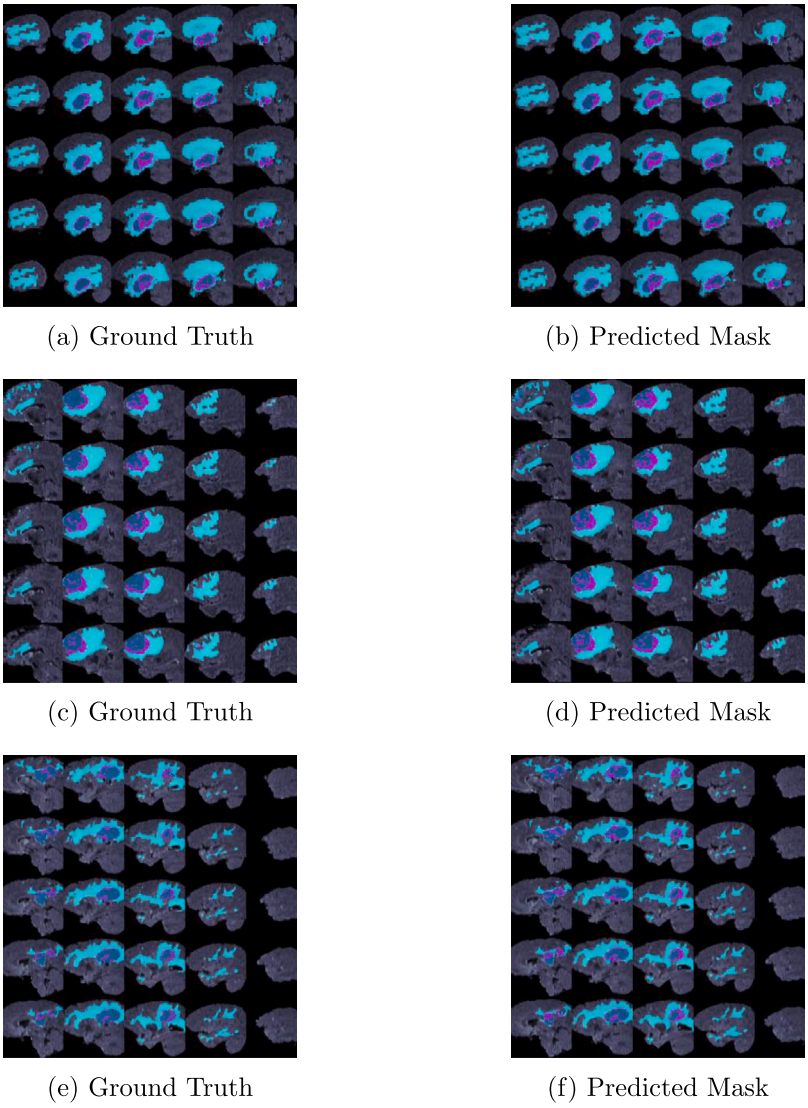

(a) Ground Truth (b) Predicted Mask

(c) Ground Truth (d) Predicted Mask

(e) Ground Truth (f) Predicted Mask

Fig. 12. Qualitative comparison of ground truth and predicted masks for three representative BraTS 2020 cases: (a)–(b) BraTS20_Training_001, (c)–(d) BraTS20_Training_006, (e)–(f) BraTS20_Training_069. Tumor subregions are color-coded as WT (Cyan), TC (Navy Blue), and ET (Magenta).

Table 4
Coefficient scores for each class obtained by testing the BraTS 2020 model with BraTS 2019 and BraTS 2018 datasets. The table displays the model's performance across different datasets, providing insights into its generalization capabilities over multiple datasets.

		WT	TC	ET
BraTS 2019	DSC	0.946	0.942	0.919
	IoU	0.902	0.905	0.862
	Sen	0.940	0.944	0.948
BraTS 2018	DSC	0.952	0.963	0.935
	IoU	0.912	0.936	0.885
	Sen	0.946	0.965	0.958

and ET, respectively, on the BraTS 2019 dataset, and 0.952, 0.963, and 0.935 on the BraTS 2018 dataset. The IoU and SEN metrics further validate the model's reliability, with stable performance across datasets. These findings underscore DSNet's potential for robust application in clinical scenarios, where consistent segmentation performance across diverse data distributions is critical.

4.4. State-of-the-art comparison

The segmentation task was performed on the BraTS 2020 dataset, and the performance of our proposed method was compared with several state-of-the-art models utilizing various versions of U-Net-based architectures. Table 5 provides a comparison of the DSC scores for different methods on the three tumor regions: WT, TC, and ET. Our model, based on a dynamic convolutional neural network and 3D adversarial learning, achieved superior results with DSC scores of 0.959 for WT, 0.975 for TC, and 0.947 for ET. The key reasons behind the higher performance of our method are its ability to effectively combine dynamic convolution operations, which adaptively adjust to different tumor features, and the use of adversarial learning, which enhances segmentation by promoting robust feature learning in challenging regions. Unlike the traditional U-Net or its variations, such as the 2D U-Net [61] and 3D U-Net [27], which rely on static convolutions or simple encoder–decoder architectures, our model benefits from a dynamic, context-sensitive approach that better captures intricate details of brain tumor structures. This is evident from our significant improvements in DSC scores, particularly in the TC region, where our method

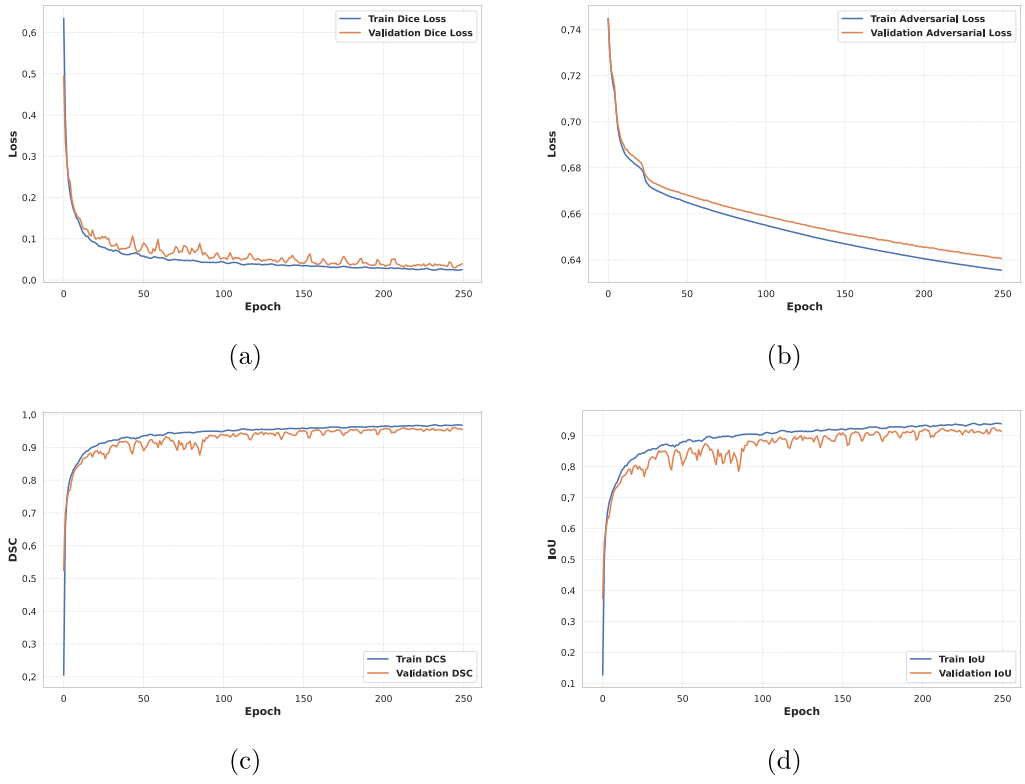

Fig. 13. Training results of our proposed model for 250 epochs using the BraTS 2019 dataset: (a) Total Loss, (b) Adversarial Loss, (c) DSC, and (d) IoU.

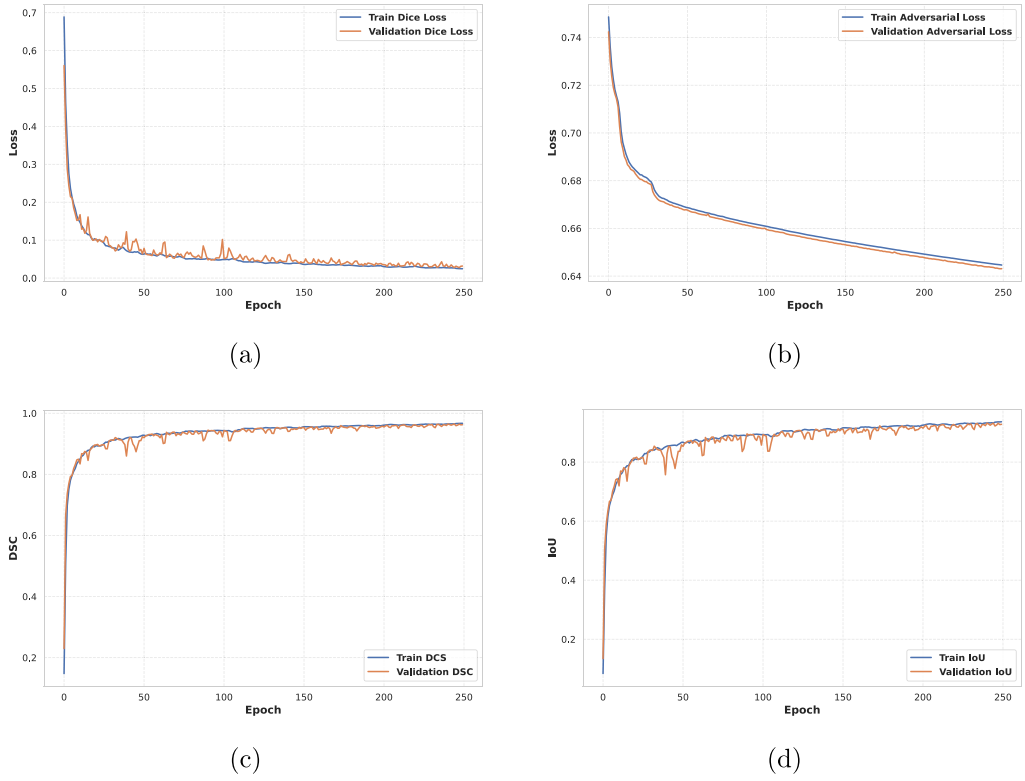

Fig. 14. Training results of our proposed model for 250 epochs using the BraTS 2018 dataset: (a) Total Loss, (b) Adversarial Loss, (c) DSC, and (d) IoU.

Table 5
DSC score comparison with various articles utilizing their versions of U-Net with BraTS 2020 dataset.

Name	Method	Validation DSC		
		WT	TC	ET
2D U-Net [61]	Their study employed a 2D CNN to create a fundamental encoder–decoder-based U-Net-type architecture.	0.867	0.798	0.751
3D U-Net [27]	The authors proposed 3D segmentation network.	0.858	0.737	0.706
Res U-Net [65]	The authors introduced a multi-pathway U-Net, which includes a residual network with skip links.	0.909	0.851	0.794
DenseTrans [66]	The authors introduces swin transformer into U-Net++ network.	0.914	0.853	0.823
GSNet [62]	The authors proposed a 3D segmentation network that combines attention-based skip connections.	0.923	0.910	0.813
TransBTS [67]	This paper introduces a novel network that uses Transformer in 3D CNN for MRI brain tumor segmentation.	0.901	0.817	0.787
SwinBTS [63]	The paper presents a method utilizing a swin-transformer, convolutional neural network, and encoder–decoder structure to predict the semantics of brain tumors.	0.891	0.803	0.773
Attention U-Net [22]	The authors proposed an attention gate model.	0.855	0.759	0.718
Cascade 3D U-Net [64]	The authors incorporated a parallel multi-scale fusion module and an expectation maximization attention mechanism into a 2-stage cascaded 3D U-Net-type model.	0.912	0.854	0.787
Proposed Method	We have employed a Dynamic Convolutional Neural Network (DCNN) and a 3D segmentation network based on adversarial learning.	**0.959**	**0.975**	**0.947**

outperforms others by a considerable margin (e.g., 0.975 vs. 0.910 in GSNet [62]). Furthermore, the integration of adversarial learning within our architecture provides a competitive edge by promoting finer boundary delineations, which is crucial for accurate tumor segmentation. This approach is demonstrated to enhance segmentation accuracy, especially in challenging areas such as the ET region, where other models such as SwinBTS [63] and Cascade 3D U-Net [64] show less favorable results. Overall, the combination of dynamic convolutions and adversarial learning makes our model more effective in handling the complexities of the BraTS 2020 dataset, achieving state-of-the-art performance across all tumor regions.

4.5. Survival prediction

In our study, we tested several state-of-the-art models to estimate survival rates, aiming to find the best-performing one. We explored different machine learning methods, including Random Forest (RF) [68], SVM [69], K-Nearest Neighbors (KNN) [70], and Multi-Layer Perceptron (MLP) [71]. Fig. 15 illustrates the training and validation accuracy for each model. The RF model outperformed the others. It achieved an accuracy of 54.6% on the validation data. To optimize the performance of the RF model, we employed grid search, a widely used hyperparameter tuning technique that exhaustively searches through a predefined set of hyperparameters to find the optimal configuration. Grid search systematically evaluates all possible combinations of specified hyperparameters, ensuring a comprehensive exploration of the parameter space [72]. Our final configuration, consisting of 50 trees each with a depth of 10, struck a satisfactory balance between generalization and accuracy.

To incorporate survival-specific analysis, we extended our evaluation to the DeepSurv model, which adapts the Cox proportional hazards framework into a deep neural network. DeepSurv achieved a concordance index (C-index) of 0.525 (bootstrapped mean: 0.528; 95% CI: 0.386–0.656), with Brier scores of 0.256 and 0.191 at 12 and 18 months, respectively. A log-rank test comparing stratified high- and low-risk groups yielded a p-value of 0.53, suggesting no statistically significant survival separation. For comparison, an RF regression model adapted for continuous survival prediction achieved a C-index of 0.507 and a mean absolute error (MAE) of approximately 327 days. While DeepSurv produced hazard-based outputs aligned with clinical interpretability, its predictive performance was similar to RF, indicating that dataset size and limited feature diversity may have constrained model discrimination.

To further enhance clinical relevance, we incorporated Shapley Additive exPlanations (SHAP)-based interpretability analysis. The SHAP summary plot (Fig. 16) highlights the relative importance of patient-level features in survival prediction, with age and volumetric fractions of enhancing, edema, and necrotic tumor regions emerging as the most influential predictors. Importantly, the analysis confirmed clinically consistent patterns—for example, older age and larger enhancing tumor volumes were strongly associated with reduced survival probability. Such insights improve model transparency, making the framework more suitable for potential clinical decision support.

4.6. Web-based application

We have created a web-based application (web app) that is user-friendly and streamlines the entire processing pipeline in order to facilitate the application of our model as a medical imaging instrument. The web application is intended to receive input in the '.nii' file format, specifically 3D MRI images. It generates segmentation masks for WT, TC, and ET regions by processing inputs from FLAIR, T1, T1ce, and T2 MRI scans, as well as the patient's age. Furthermore, it forecasts the severity of the patient's condition. The web application is capable of producing and locally saving segmentation masks in the '.nii' file format within 40 s, ensuring rapid performance. This rapidity is essential in clinical environments, where treatment decisions can be significantly influenced by opportune analysis. The application is accessible through a web browser at "http://127.0.0.1:5000/" and is hosted on a local system.

In the web application input page, users can upload the necessary MRI scans and insert the patient's age. The web application processes the data and generates the output segmentation masks after providing the inputs. Subsequently, these outputs are stored in a designated local

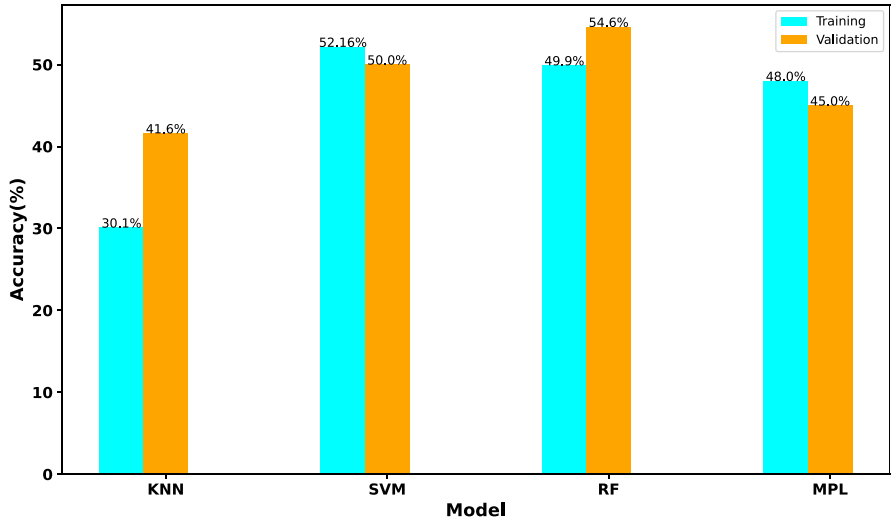

Fig. 15. Comparison of training and validation accuracies for various machine learning models (SVM, RF, KNN, and MLP) in the survival prediction task. The bar plot illustrates the performance of each model, highlighting the differences in accuracy between the training data (blue bars) and the validation data (orange bars), thereby providing insights into each model's generalization capability.

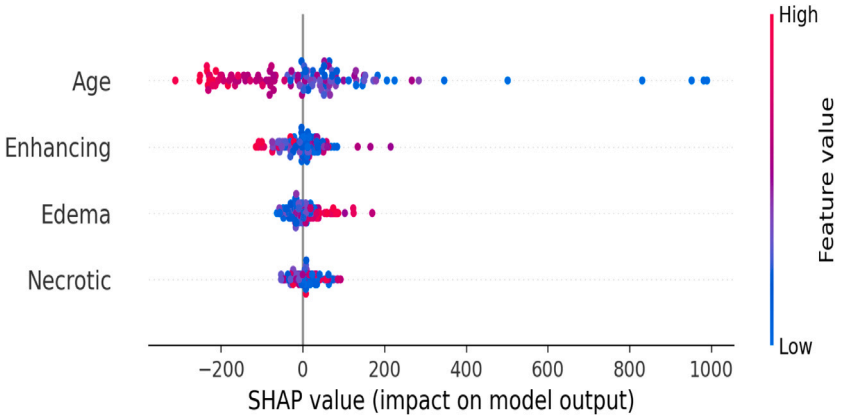

Fig. 16. SHAP beeswarm summary plot for the survival prediction model. Features are ordered by importance, and each point represents a patient. The x-axis shows the SHAP value (impact on model output), while the color gradient denotes feature values (red = high, blue = low). Age and tumor subregion fractions emerged as the most influential predictors.

folder. This web application not only improves the efficiency and effectiveness of medical imaging analysis in clinical practice but also enables healthcare professionals to employ sophisticated AI tools without the need for extensive technical expertise. Additionally, it simplifies the process of medical image segmentation.

The current implementation exclusively uses publicly available, fully de-identified BraTS datasets, which contain no patient-identifiable information, thereby inherently complying with GDPR and HIPAA requirements [73]. For potential clinical deployment, the system can be extended to ensure full regulatory compliance by incorporating secure data encryption, strict access control, anonymization of any identifiable information, and adherence to institutional data retention/deletion policies. The complete source code, trained model weights, and setup instructions for running the Web application have been made publicly available on GitHub https://github.com/AshfakYeafi/DSNet [74]. This Web application is a research prototype intended for local single-user use to demonstrate the feasibility of the DSNet pipeline. Comprehensive scalability testing under varied network conditions and concurrent workloads lies beyond the present study's scope and will be explored in future work.

5. Discussion

This study demonstrates that the proposed DSNet framework achieves state-of-the-art performance in brain tumor segmentation by effectively integrating DCNNs with adversarial learning. Experimental results across multiple BraTS benchmarks confirm DSNet's superiority over existing approaches and highlight its translational potential for neuro-oncology. A major factor contributing to this success is the incorporation of dynamic convolutional layers, which allow the network to adapt its filters to the heterogeneous spatial and structural properties of tumor regions. Conventional static convolutions often struggle with irregular morphologies, whereas dynamic convolutions enhance boundary delineation, particularly for the TC and ET. This

adaptive mechanism addresses a long-standing limitation of CNN-based segmentation methods and improves fine-grained localization of complex tumor structures.

The addition of adversarial learning further strengthens segmentation quality by encouraging the generator to produce maps that closely approximate expert annotations. This strategy reduces discontinuities and artifacts, thereby ensuring spatial coherence across the WT, TC, and ET regions. Such improvements directly counter a well-documented shortcoming of deterministic CNNs, which frequently generate outputs lacking realism in heterogeneous or high-variance regions.

DSNet also exhibits strong generalization capacity, as demonstrated by consistent performance on BraTS 2018, 2019, and 2020 datasets. High Dice and IoU scores suggest robustness to varying data distributions without extensive retraining, a property essential for clinical translation. However, since training and validation were restricted to BraTS cohorts, potential dataset-specific biases remain. Future studies will therefore extend evaluation to multi-institutional datasets such as TCIA and ISLES to assess cross-center generalizability more rigorously. Although class imbalance was a challenge, stratified k-fold cross-validation partially mitigated its effects. To further address this limitation, future work will explore targeted augmentation strategies such as elastic deformations and GAN-based patch synthesis, which may improve the representation of under-represented lesion types.

Quantitatively, DSNet achieved Dice scores of 0.959 (WT), 0.975 (TC), and 0.947 (ET), outperforming leading segmentation models including U-Net, Attention U-Net, ResU-Net, TransBTS, SwinBTS, and Cascade 3D U-Net. Nonetheless, more comprehensive evaluations are necessary. Metrics such as the Hausdorff distance and statistical significance testing could provide stronger evidence of superiority but require raw predictions from competing models, which are not currently accessible. Future benchmarking efforts will prioritize these analyses.

Beyond segmentation, DSNet was extended with a survival prediction module, further demonstrating its clinical utility. In this framework, volumetric features derived from DSNet's segmentation outputs were used to train an RF classifier for patient outcome modeling. Unlike deep learning models, the RF offers a practical balance between interpretability and predictive accuracy, making it particularly suitable for clinical contexts where explainability is essential. To enhance predictive performance, a grid search was employed for hyperparameter tuning, improving the model's ability to estimate survival outcomes. Despite these optimizations, predictive accuracy remained limited due to the small size of the available survival dataset. This limitation underscores the importance of incorporating larger and more diverse clinical cohorts in future studies to improve robustness, reliability, and clinical applicability. To incorporate survival-specific modeling, the DeepSurv framework—an adaptation of the Cox proportional hazards model into a deep neural network was also evaluated. While DeepSurv produced hazard-based outputs that aligned well with clinical interpretation, its predictive performance was comparable to RF, again highlighting dataset size and feature diversity as key limitations in model discrimination. To improve transparency and clinical trust, SHAP-based interpretability analysis was applied to both survival models. This analysis revealed clinically consistent patterns, such as older age and larger enhancing tumor volumes being strongly associated with reduced survival probability. Such insights enhance the transparency of the survival modeling framework and underscore its potential as a clinically relevant decision-support tool when combined with more comprehensive datasets.

Finally, the deployment of DSNet through a lightweight web application demonstrates its translational potential by providing clinicians with a user-friendly tool capable of segmenting 3D MRI scans and generating survival predictions in under one minute. This design bridges the gap between algorithmic development and real-world applicability, aligning with the time-sensitive nature of clinical decision-making. In summary, DSNet's contributions lie in its dynamic convolutional design, adversarial learning integration, demonstrated generalization across multiple datasets, and practical deployment for clinical use. By explicitly acknowledging limitations and outlining avenues for external validation, advanced augmentation, and rigorous statistical benchmarking, this work positions DSNet as both a competitive and extensible framework for precision neuro-oncology applications.

6. Conclusion

This study presents DSNet, a robust framework for brain tumor analysis that enhances 3D U-Net performance through adversarial learning, dynamic convolutional layers, attention mechanisms, and residual connections. Applied to multimodal MRI data, DSNet achieves superior segmentation accuracy and robustness, validated by consistently high Dice scores across tumor subregions. In addition to segmentation, the proposed methodology includes a survival prediction component that leverages both radiographic and clinical features to generate individualized prognostic assessments using machine learning techniques. The development of a user-friendly graphical interface (GUI) further facilitates real-world adoption, enabling interactive visualization and efficient integration into clinical workflows. By combining advanced segmentation, predictive modeling, and user-centered design, DSNet delivers a comprehensive, clinically relevant solution that advances the precision, interpretability, and utility of brain tumor diagnosis and prognosis.

Future work will focus on enhancing model generalizability by incorporating multi-institutional and real-world clinical datasets. Expanding the framework to support longitudinal analysis could enable monitoring of tumor progression over time. Additionally, developing explainable AI components can enhance clinical interpretability and trust. Finally, real-world validation of the proposed GUI in clinical workflows will be pursued to assess usability and facilitate broader adoption.

Declaration of competing interest

The authors declare that they have no known competing financial interests or personal relationships that could have appeared to influence the work reported in this paper.

Data availability

Data will be made available on request.

References

[1] Ashfak Yeafi, Monira Islam, Sohag Kumar Mondal, KM Ishraq Hussain Nashad, Md Salah Uddin Yusuf, A semi-supervised approach for brain tumor classification using wasserstein generative adversarial network with gradient penalty, in: 2023 6th International Conference on Electrical Information and Communication Technology, EICT, IEEE, 2023, pp. 1–6.

[2] National Brain Tumor Society (NBTS), National brain tumor society, 2008, U.S. nonprofit organization focused on brain tumor research and patient support. https://www.braintumor.org/.

[3] Saddam Hussain, Syed Muhammad Anwar, Muhammad Majid, Segmentation of glioma tumors in brain using deep convolutional neural network, Neurocomputing 282 (2018) 248–261.

[4] Shah Hussain, Iqra Mubeen, Niamat Ullah, Syed Shahab Ud Din Shah, Bakhtawar Abduljalil Khan, Muhammad Zahoor, Riaz Ullah, Farhat Ali Khan, Mujeeb A Sultan, Modern diagnostic imaging technique applications and risk factors in the medical field: a review, BioMed Res. Int. 2022 (1) (2022) 5164970.

[5] Florian Alexander Huber, Filippo Del Grande, Stefania Rizzo, Giuseppe Guglielmi, Roman Guggenberger, MRI in the assessment of adipose tissues and muscle composition: how to use it, Quant. Imaging Med. Surg. 10 (8) (2020) 1636.

[6] Andreas S Panayides, Amir Amini, Nenad D Filipovic, Ashish Sharma, Sotirios A Tsaftaris, Alistair Young, David Foran, Nhan Do, Spyretta Golemati, Tahsin Kurc, et al., AI in medical imaging informatics: current challenges and future directions, IEEE J. Biomed. Heal. Inform. 24 (7) (2020) 1837–1857.

[7] Asieh Khosravanian, Mohammad Rahmanimanesh, Parviz Keshavarzi, Saeed Mozaffari, Fast level set method for glioma brain tumor segmentation based on superpixel fuzzy clustering and lattice Boltzmann method, Comput. Methods Programs Biomed. 198 (2021) 105809.

[8] Zhenyu Tang, Sahar Ahmad, Pew-Thian Yap, Dinggang Shen, Multi-atlas segmentation of MR tumor brain images using low-rank based image recovery, IEEE Trans. Med. Imaging 37 (10) (2018) 2224–2235.

[9] Shanshan Wang, Cheng Li, Rongpin Wang, Zaiyi Liu, Meiyun Wang, Hongna Tan, Yaping Wu, Xinfeng Liu, Hui Sun, Rui Yang, et al., Annotation-efficient deep learning for automatic medical image segmentation, Nat. Commun. 12 (1) (2021) 5915.

[10] Keiron O'shea, Ryan Nash, An introduction to convolutional neural networks, 2015, arXiv preprint arXiv:1511.08458.

[11] Olaf Ronneberger, Philipp Fischer, Thomas Brox, U-net: Convolutional networks for biomedical image segmentation, in: Medical Image Computing and Computer-Assisted Intervention–MICCAI 2015: 18th International Conference, Munich, Germany, October 5-9, 2015, Proceedings, Part III 18, Springer, 2015, pp. 234–241.

[12] Qi Dou, Lequan Yu, Hao Chen, Yueming Jin, Xin Yang, Jing Qin, Pheng-Ann Heng, 3D deeply supervised network for automated segmentation of volumetric medical images, Med. Image Anal. 41 (2017) 40–54.

[13] Georgios Zoumpourlis, Alexandros Doumanoglou, Nicholas Vretos, Petros Daras, Non-linear convolution filters for CNN-based learning, in: Proceedings of the IEEE International Conference on Computer Vision, 2017, pp. 4761–4769.

[14] Yinpeng Chen, Xiyang Dai, Mengchen Liu, Dongdong Chen, Lu Yuan, Zicheng Liu, Dynamic convolution: Attention over convolution kernels, in: Proceedings of the IEEE/CVF Conference on Computer Vision and Pattern Recognition, 2020, pp. 11030–11039.

[15] Ahmed Iqbal, Muhammad Sharif, Mussarat Yasmin, Mudassar Raza, Shabib Aftab, Generative adversarial networks and its applications in the biomedical image segmentation: a comprehensive survey, Int. J. Multimed. Inf. Retr. 11 (3) (2022) 333–368.

[16] Siyi Xun, Dengwang Li, Hui Zhu, Min Chen, Jianbo Wang, Jie Li, Meirong Chen, Bing Wu, Hua Zhang, Xiangfei Chai, et al., Generative adversarial networks in medical image segmentation: A review, Comput. Biol. Med. 140 (2022) 105063.

[17] Xue Dong, Yang Lei, Tonghe Wang, Matthew Thomas, Leonardo Tang, Walter J Curran, Tian Liu, Xiaofeng Yang, Automatic multiorgan segmentation in thorax CT images using U-net-GAN, Med. Phys. 46 (5) (2019) 2157–2168.

[18] Tirivangani Magadza, Serestina Viriri, Deep learning for brain tumor segmentation: a survey of state-of-the-art, J. Imaging 7 (2) (2021) 19.

[19] B. Basavaprasad, S. Hegadi Ravindra, A survey on traditional and graph theoretical techniques for image segmentation, Int. J. Comput. Appl 975 (2014) 8887.

[20] Shervin Minaee, Yuri Boykov, Fatih Porikli, Antonio Plaza, Nasser Kehtarnavaz, Demetri Terzopoulos, Image segmentation using deep learning: A survey, IEEE Trans. Pattern Anal. Mach. Intell. 44 (7) (2021) 3523–3542.

[21] Zongwei Zhou, Md Mahfuzur Rahman Siddiquee, Nima Tajbakhsh, Jianming Liang, Unet++: A nested u-net architecture for medical image segmentation, in: Deep Learning in Medical Image Analysis and Multimodal Learning for Clinical Decision Support: 4th International Workshop, DLMIA 2018, and 8th International Workshop, ML-CDS 2018, Held in Conjunction with MICCAI 2018, Granada, Spain, September 20, 2018, Proceedings 4, Springer, 2018, pp. 3–11.

[22] Ozan Oktay, Jo Schlemper, Loic Le Folgoc, Matthew Lee, Mattias Heinrich, Kazunari Misawa, Kensaku Mori, Steven McDonagh, Nils Y Hammerla, Bernhard Kainz, et al., Attention U-net: Learning where to look for the pancreas, 2018, arXiv preprint arXiv:1804.03999.

[23] Xiao Xiao, Shen Lian, Zhiming Luo, Shaozi Li, Weighted res-unet for high-quality retina vessel segmentation, in: 2018 9th International Conference on Information Technology in Medicine and Education, ITME, IEEE, 2018, pp. 327–331.

[24] Jason Walsh, Alice Othmani, Mayank Jain, Soumyabrata Dev, Using U-Net network for efficient brain tumor segmentation in MRI images, Heal. Anal. 2 (2022) 100098.

[25] Cheng-Jui Tseng, Changjiang Tang, An optimized XGBoost technique for accurate brain tumor detection using feature selection and image segmentation, Heal. Anal. 4 (2023) 100217.

[26] Kamini Lamba, Shalli Rani, Monika Anand, Lakshmana Phaneendra Maguluri, An integrated deep learning and supervised learning approach for early detection of brain tumor using magnetic resonance imaging, Heal. Anal. 5 (2024) 100336.

[27] Özgün Çiçek, Ahmed Abdulkadir, Soeren S Lienkamp, Thomas Brox, Olaf Ronneberger, 3D U-Net: learning dense volumetric segmentation from sparse annotation, in: Medical Image Computing and Computer-Assisted Intervention–MICCAI 2016: 19th International Conference, Athens, Greece, October 17-21, 2016, Proceedings, Part II 19, Springer, 2016, pp. 424–432.

[28] Ian Goodfellow, Jean Pouget-Abadie, Mehdi Mirza, Bing Xu, David Warde-Farley, Sherjil Ozair, Aaron Courville, Yoshua Bengio, Generative adversarial nets, Adv. Neural Inf. Process. Syst. 27 (2014).

[29] Marco Domenico Cirillo, David Abramian, Anders Eklund, Vox2Vox: 3D-GAN for brain tumour segmentation, in: Brainlesion: Glioma, Multiple Sclerosis, Stroke and Traumatic Brain Injuries: 6th International Workshop, BrainLes 2020, Held in Conjunction with MICCAI 2020, Lima, Peru, October 4, 2020, Revised Selected Papers, Part I 6, Springer, 2021, pp. 274–284.

[30] Himashi Peiris, Zhaolin Chen, Gary Egan, Mehrtash Harandi, Reciprocal adversarial learning for brain tumor segmentation: a solution to BraTS challenge 2021 segmentation task, in: International MICCAI Brainlesion Workshop, Springer, 2021, pp. 171–181.

[31] Asifullah Khan, Zunaira Rauf, Abdul Rehman Khan, Saima Rathore, Saddam Hussain Khan, Najmus Saher Shah, Umair Farooq, Hifsa Asif, Aqsa Asif, Umme Zahoora, et al., A recent survey of vision transformers for medical image segmentation, 2023, arXiv preprint arXiv:2312.00634.

[32] Jessica Valdebenito, Felipe Medina, Machine learning approaches to study glioblastoma: A review of the last decade of applications, Cancer Rep. 2 (6) (2019) e1226.

[33] Bjoern H Menze, Andras Jakab, Stefan Bauer, Jayashree Kalpathy-Cramer, Keyvan Farahani, Justin Kirby, Yuliya Burren, Nicole Porz, Johannes Slotboom, Roland Wiest, et al., The multimodal brain tumor image segmentation benchmark (BRATS), IEEE Trans. Med. Imaging 34 (10) (2014) 1993–2024.

[34] Spyridon Bakas, Hamed Akbari, Aristeidis Sotiras, Michel Bilello, Martin Rozycki, Justin S Kirby, John B Freymann, Keyvan Farahani, Christos Davatzikos, Advancing the cancer genome atlas glioma MRI collections with expert segmentation labels and radiomic features, Sci. Data 4 (1) (2017) 1–13.

[35] Spyridon Bakas, Mauricio Reyes, Andras Jakab, Stefan Bauer, Markus Rempfler, Alessandro Crimi, Russell Takeshi Shinohara, Christoph Berger, Sung Min Ha, Martin Rozycki, et al., Identifying the best machine learning algorithms for brain tumor segmentation, progression assessment, and overall survival prediction in the BRATS challenge, 2018, arXiv preprint arXiv:1811.02629.

[36] Meenu Bhagat, Brijesh Bakariya, Implementation of logistic regression on diabetic dataset using train-test-split, k-fold and stratified k-fold approach, Nat. Acad. Sci. Lett. 45 (5) (2022) 401–404.

[37] T-W Ke, Aaron S Brewster, Stella X Yu, Daniela Ushizima, Chao Yang, Nicholas K Sauter, A convolutional neural network-based screening tool for X-ray serial crystallography, J. Synchrotron Radiat. 25 (3) (2018) 655–670.

[38] Justin Suh Paul, Dong-Hyun Hwang, Sung-Hong Park, Deep learning for brain tumor classification, Med. Imaging Technol. 35 (5) (2017) 260–268.

[39] Sergio Pereira, Adriano Pinto, Victor Alves, Carlos A Silva, Brain tumor segmentation using convolutional neural networks in mri images, IEEE Trans. Med. Imaging 35 (5) (2016) 1240–1251.

[40] Bjoern H Menze, Andras Jakab, Stefan Bauer, Jayashree Kalpathy-Cramer, Keyvan Farahani, et al., The multimodal brain tumor image segmentation benchmark (BRATS), IEEE Trans. Med. Imaging 34 (10) (2015) 1993–2024.

[41] Shu Liu, Lu Qi, Haifang Qin, Jianping Shi, Jiaya Jia, Path aggregation network for instance segmentation, in: Proceedings of the IEEE Conference on Computer Vision and Pattern Recognition, 2018, pp. 8759–8768.

[42] Shuiwang Ji, Wei Xu, Ming Yang, Kai Yu, 3D convolutional neural networks for human action recognition, IEEE Trans. Pattern Anal. Mach. Intell. 35 (1) (2012) 221–231.

[43] Rajarshi Haldar, Lingfei Wu, Jinjun Xiong, Julia Hockenmaier, A multi-perspective architecture for semantic code search, 2020, arXiv preprint arXiv:2005.06980.

[44] Sergey Ioffe, Christian Szegedy, Batch normalization: Accelerating deep network training by reducing internal covariate shift, in: International Conference on Machine Learning, PMLR, 2015, pp. 448–456.

[45] Kaiming He, Xiangyu Zhang, Shaoqing Ren, Jian Sun, Deep residual learning for image recognition, in: Proceedings of the IEEE Conference on Computer Vision and Pattern Recognition, 2016, pp. 770–778.

[46] Ashish Vaswani, Noam Shazeer, Niki Parmar, Jakob Uszkoreit, Llion Jones, Aidan N Gomez, Łukasz Kaiser, Illia Polosukhin, Attention is all you need, Adv. Neural Inf. Process. Syst. 30 (2017).

[47] Hidenori Ide, Takio Kurita, Improvement of learning for CNN with ReLU activation by sparse regularization, in: 2017 International Joint Conference on Neural Networks, IJCNN, IEEE, 2017, pp. 2684–2691.

[48] Andrew L. Maas, Awni Y. Hannun, Andrew Y. Ng, et al., Rectifier nonlinearities improve neural network acoustic models, in: Proc. Icml, vol. 30, (1) Atlanta, GA, 2013, p. 3.

[49] Sagar Sharma, Simone Sharma, Anidhya Athaiya, Activation functions in neural networks, Towar. Data Sci 6 (12) (2017) 310–316.

[50] Hyeonwoo Noh, Seunghoon Hong, Bohyung Han, Learning deconvolution network for semantic segmentation, in: Proceedings of the IEEE International Conference on Computer Vision, 2015, pp. 1520–1528.

[51] Phillip Isola, Jun-Yan Zhu, Tinghui Zhou, Alexei A Efros, Image-to-image translation with conditional adversarial networks, in: Proceedings of the IEEE Conference on Computer Vision and Pattern Recognition, 2017, pp. 1125–1134.

[52] Chuan Li, Michael Wand, Precomputed real-time texture synthesis with markovian generative adversarial networks, in: Computer Vision–ECCV 2016: 14th European Conference, Amsterdam, the Netherlands, October 11-14, 2016, Proceedings, Part III 14, Springer, 2016, pp. 702–716.

[53] Jared L Katzman, Uri Shaham, Alexander Cloninger, Jonathan Bates, Tingting Jiang, Yuval Kluger, DeepSurv: personalized treatment recommender system using a Cox proportional hazards deep neural network, BMC Med. Res. Methodol. 18 (1) (2018) 24.

[54] Zijun Zhang, Improved adam optimizer for deep neural networks, in: 2018 IEEE/ACM 26th International Symposium on Quality of Service, IWQoS, IEEE, 2018, pp. 1–2.

[55] Geoffrey Hinton, Nitish Srivastava, Kevin Swersky, Neural networks for machine learning lecture 6a overview of mini-batch gradient descent, Cited on 14 (8) (2012) 2.
[56] Marco Gori, Alberto Tesi, et al., On the problem of local minima in backpropagation, IEEE Trans. Pattern Anal. Mach. Intell. 14 (1) (1992) 76–86.
[57] Tom Eelbode, Jeroen Bertels, Maxim Berman, Dirk Vandermeulen, Frederik Maes, Raf Bisschops, Matthew B Blaschko, Optimization for medical image segmentation: theory and practice when evaluating with dice score or jaccard index, IEEE Trans. Med. Imaging 39 (11) (2020) 3679–3690.
[58] Agung W. Setiawan, Image segmentation metrics in skin lesion: accuracy, sensitivity, specificity, dice coefficient, jaccard index, and matthews correlation coefficient, in: 2020 International Conference on Computer Engineering, Network, and Intelligent Multimedia, CENIM, IEEE, 2020, pp. 97–102.
[59] M. Krithika Alias AnbuDevi, K. Suganthi, Review of semantic segmentation of medical images using modified architectures of UNET, Diagnostics 12 (12) (2022) 3064.
[60] Lina Huang, Alina Miron, Kate Hone, Yongmin Li, Segmenting medical images: From UNet to Res-UNet and nnUNet, in: 2024 IEEE 37th International Symposium on Computer-Based Medical Systems, CBMS, IEEE, 2024, pp. 483–489.
[61] Jordan Colman, Lei Zhang, Wenting Duan, Xujiong Ye, DR-Unet104 for multimodal MRI brain tumor segmentation, in: Brainlesion: Glioma, Multiple Sclerosis, Stroke and Traumatic Brain Injuries: 6th International Workshop, BrainLes 2020, Held in Conjunction with MICCAI 2020, Lima, Peru, October 4, 2020, Revised Selected Papers, Part II 6, Springer, 2021, pp. 410–419.
[62] Md Tasnim Jawad, Ashfak Yeafi, Kalyan Kumar Halder, GSNet: a multi-class 3D attention-based hybrid glioma segmentation network, Opt. Express 31 (24) (2023) 40881–40906.
[63] Yun Jiang, Yuan Zhang, Xin Lin, Jinkun Dong, Tongtong Cheng, Jing Liang, SwinBTS: A method for 3D multimodal brain tumor segmentation using swin transformer, Brain Sci. 12 (6) (2022) 797.
[64] Haozhe Jia, Weidong Cai, Heng Huang, Yong Xia, Hˆ 2 2 NF-Net for brain tumor segmentation using multimodal mr imaging: 2nd place solution to brats challenge 2020 segmentation task, in: Brainlesion: Glioma, Multiple Sclerosis, Stroke and Traumatic Brain Injuries: 6th International Workshop, BrainLes 2020, Held in Conjunction with MICCAI 2020, Lima, Peru, October 4, 2020, Revised Selected Papers, Part II 6, Springer, 2021, pp. 58–68.
[65] Aheli Saha, Yu-Dong Zhang, Suresh Chandra Satapathy, Brain tumour segmentation with a muti-pathway ResNet based UNet, J. Grid Comput. 19 (2021) 1–10.
[66] Li ZongRen, Wushouer Silamu, Wang Yuzhen, Wei Zhe, DenseTrans: multimodal brain tumor segmentation using swin transformer, IEEE Access 11 (2023) 42895–42908.
[67] Wang Wenxuan, Chen Chen, Ding Meng, Yu Hong, Zha Sen, Li Jiangyun, Transbts: Multimodal brain tumor segmentation using transformer, in: International Conference on Medical Image Computing and Computer-Assisted Intervention, Springer, 2021, pp. 109–119.
[68] Mahesh Pal, Random forest classifier for remote sensing classification, Int. J. Remote Sens. 26 (1) (2005) 217–222.
[69] Richard G. Brereton, Gavin R. Lloyd, Support vector machines for classification and regression, Analyst 135 (2) (2010) 230–267.
[70] Gongde Guo, Hui Wang, David Bell, Yaxin Bi, Kieran Greer, KNN model-based approach in classification, in: On the Move To Meaningful Internet Systems 2003: CoopIS, DOA, and ODBASE: OTM Confederated International Conferences, CoopIS, DOA, and ODBASE 2003, Catania, Sicily, Italy, November 3-7, 2003. Proceedings, Springer, 2003, pp. 986–996.
[71] B.B. Chaudhuri, Ujjwal Bhattacharya, Efficient training and improved performance of multilayer perceptron in pattern classification, Neurocomputing 34 (1–4) (2000) 11–27.
[72] Marc-André Zöller, Marco F. Huber, Benchmark and survey of automated machine learning frameworks, J. Artificial Intelligence Res. 70 (2021) 409–472.
[73] Office for Civil Rights, Guidance regarding methods for de-identification of protected health information in accordance with the health insurance portability and accountability act (HIPAA) privacy rule, 2012,
[74] Web App installation, https://github.com/AshfakYeafi/DSNet/blob/main/README.md.